Version of Record: https://www.sciencedirect.com/science/article/pii/S0013794416305173
ed720f8419f33ccc31eb31e75d79049e

Animprovedinterfacial bonding model for material interface modeling

Liqiang Lin, Xiaodu Wang, Xiaowei Zeng*

Department of Mechanical Engineering, University of Texas at San Antonio, TX 78249

Abstract: Animproved interfacial bonding model was proposed from potential function point of view to investigate interfacial interactions in polycrystalline materials.It characterizes both attractive and repulsive interfacial interactions and can be applied to model different material interfaces. The path dependence of work-of-separation study indicates that the transformation of separation work is smooth in normal and tangential direction and the proposed modelguarantees the consistency of the cohesive constitutive model. The improved interfacial bonding model was verified through a simple compression test in a standard hexagonal structure. The error between analytical solutions and numerical results from the proposed model is reasonable in linear elastic region. Ultimately, we investigated the mechanical behavior of extrafibrillar matrix in bone and the simulation results agreed well with experimental observations of bone fracture.

Keywords: Material interface modeling;Interfacial bonding model; Finite Element simulation;Polycrystalline structure;Bone fracture

1. Introduction

The bulk mechanical behavior ofa material is largely determined by its microstructures, e.g. grain and grain boundaries in polycrystalline materials, bi-material interface in composite materials. For instance, in natural staggered composites such as bone and nacre, the brittle tablets are bonded by softer interfaces capable of dissipating a significant amount of energy[1], which makes the material remarkably strong and tough. Therefore, how to characterize and model these interfacial zones has been the focus of intense research. A significant amount of research efforts are being dedicated to develop interfacial zone models, mainly in the simulation of materials failure. The coupled atomistic/continuum interface zone models were developed for the

* Corresponding author. Tel.: +1 210 458 7698
E-mail address: xiaowei.zeng@utsa.edu (X. Zeng)

analysis of dynamically propagating crack of interfaces [2-4].Gao and Klein[5] proposed a virtual internal bond (VIB) modelwith randomized cohesive interactions between material particles. This VIB model incorporates an atomic cohesive force law into the constitutive model of materials for modeling deformation and failure in the interfacial region.Additionally, different cohesive zone models were developed todescribe interfacial behaviorsfor material failure analysis [6-10].

Amongdifferent cohesive zone models, the exponential cohesive zone model [7] is one of the most popular interfacial zone models. The constitutive relationship of cohesive fracture is described by a potential in the model, which characterizes the physical debonding behavior. Although the exponential cohesive zone model has gained much popularity in material failure simulations, it has several limitations. It is often based on the assumption that the normal fracture energy equals the shear fracture energy [11-13]. This assumption is often not consistent with the experiment proof. In fact, multiple experimental studies indicated that the fracture energies in modes I and mode II are different, e.g. Araki et al. [14], Benzeggagh and Kenane[15], Dollhofer et al. [16], Pang [17], Warrior et al. [18] and Yang et al. [19]. Furthermore, when the interface is under a large normal compression condition, the maximum shear traction T_t^* will become negative and this does not appear to be realistic [20]. In addition, with large tangential separation, the maximum normal repulsive traction $-T_n^*$ will decrease to zero, which might result in surface penetration of two contact surfaces under large compressive displacement.

The original exponential cohesive zone model [7]has been extended and altered by many researchers for different applications. An irreversible exponential cohesive zone model that uses an effective opening displacement was developed by Ortiz and Pandolfi[21] to consider different ratio of tractions along sliding and normal direction under mixed-mode failure. Later, Zhang and Paulino[22] extended the original exponential cohesive zone model to functionally graded materials(FGMs)modeling, which considers the influence of material gradation on crack initiation in mixed-mode fracture problem. Van den Bosch et al. [20] adopted the original exponential cohesive zone model as a mixed-mode exponential cohesive zone model with different normal and shear fracture energy. Recently, Zeng and Li [23] developed a multiscale cohesive zone model, in which the cohesive laws can be obtained from atomic lattice structures.

In this paper, animproved interfacialbonding model was proposedto address the aforementioned problems and to study the interfacial interactions in biological materials, especially to model the organic interface of extrafibrillar matrix in bone. The mechanical responses of bone not only depend on its microstructure, but also depend on different loading conditions [24]. Current experimental studies on bone fracture are mainly in tension or bending tests because it is easy to conduct those tests. Only limited knowledge is available on the mechanical response of bone under compressive loading. In fact, bones in life are usually loaded in compression although they can fail at any loading direction[25, 26]. A few experiments have been conducted to understand the mechanism of bone failure in compression[24, 27, 28]. However, due to the complex character of bone failure under compression [24, 25],it is difficult to pinpoint the key characteristic of bone failure under compression, e.g. shear damage or slippage interaction between collagen and mineral phase causing the irreversible deformation. Therefore, it is necessary to develop numerical models to study bone failure mechanisms under compressive loading. This model was developed from a potential function andit characterizes different potentials/fracture energies, different interfacial strengths and describes attractive and repulsive behaviors of interfacial interactions.This improved interfacial bonding model not only preserves all essential features of an improved exponential cohesive zone model[20], it is also physicallyrealisticwith interface under both tension and compressioncondition. Furthermore, the proposed interfacialbonding model was verified through a simple compression test in a standard hexagonal structure.Ultimately, theproposed interfacialbonding model wasemployed to study the mechanical behavior of the extrafibrillar matrix in bone.

The paper is organized in sevenSections: in Section 2, the traditional exponential cohesive zone model was reviewed; in Section 3, the improved interfacial bonding model was developed; in Section 4, path dependence of work-of-separation of the improved interfacial bonding model wasstudied; Section 5verified the proposed model by analytical solutions; in Section 6, a fracture simulation ofextrafibrillar matrix in bonewas presented; and Section 7concluded the present work.

2. Exponential cohesive zone model

Based on a fit to atomistic calculations, the specific fracture energy φ on inter-surfaces between bulks in the exponential cohesive zone model is given by [7]:

$$\varphi(\Delta) = \varphi_0 + \varphi_0 \exp(1) - \frac{\Delta_n}{\delta_n}\left\{\left[1 - r + \frac{\Delta_n}{\delta_n}\right]\frac{1-q}{r-1} - \left[q + \left(\frac{r-q}{r-1}\right)\frac{\Delta_n}{\delta_n}\right] exp\left(-\frac{\Delta_t^2}{\delta_t^2}\right)\right\} (1)$$

Where δ_n and δ_t represent normal and shear characteristiclengths related to the debonding process, respectively and r is defined as:

$$r = \frac{\Delta_n^*}{\delta_n}$$

where,Δ_n^* is the value of Δ_n after complete shear separation with $T_n = 0$

To yieldthe realistic results of mixed-mode condition, it is necessary to set$q = 1$ at potential state. Thus, the potential can be written as[20, 29]:

$$\varphi(\Delta) = \varphi_0 - \varphi_0 \exp(1) - \frac{\Delta_n}{\delta_n}\left(1 + \frac{\Delta_n}{\delta_n}\right) exp\left(-\frac{\Delta_t^2}{\delta_t^2}\right) (2)$$

Differentiating Eq.(2) with respect to Δ_n and Δ_t yields the tractions, respectively, in normal and tangential directions as:

$$T_n = \frac{\partial\varphi(\Delta)}{\partial\Delta_n} = \frac{\varphi_n \Delta_n}{\delta_n^2} exp\left(-\frac{\Delta_n}{\delta_n}\right) exp\left(-\frac{\Delta_t^2}{\delta_t^2}\right) (3)$$

$$T_t = \frac{\partial\varphi(\Delta)}{\partial\Delta_t} = \frac{2\varphi_t \Delta_t}{\delta_t^2}\left(1 + \frac{\Delta_n}{\delta_n}\right) exp\left(-\frac{\Delta_n}{\delta_n}\right) exp\left(-\frac{\Delta_t^2}{\delta_t^2}\right) (4)$$

where $\delta_n = \frac{\varphi_n}{exp(1)\sigma_c}$, $\delta_t = \frac{\varphi_t\sqrt{\frac{2}{\exp(1)}}}{\tau_c}$, σ_c is the normal strength, τ_c is the shear strength and exp(1)=2.71828. The normal traction T_n as a function of Δ_n across the surface in the condition of $\Delta_t = 0$ is illustrated in Fig. 1(a). The value of T_n will reach maximum stress σ_c when $\Delta_n = \delta_n$ and then decrease to zero. Fig. 1(b) displays the shear traction T_t as a function of $\Delta_t$with $\Delta_n = 0$.

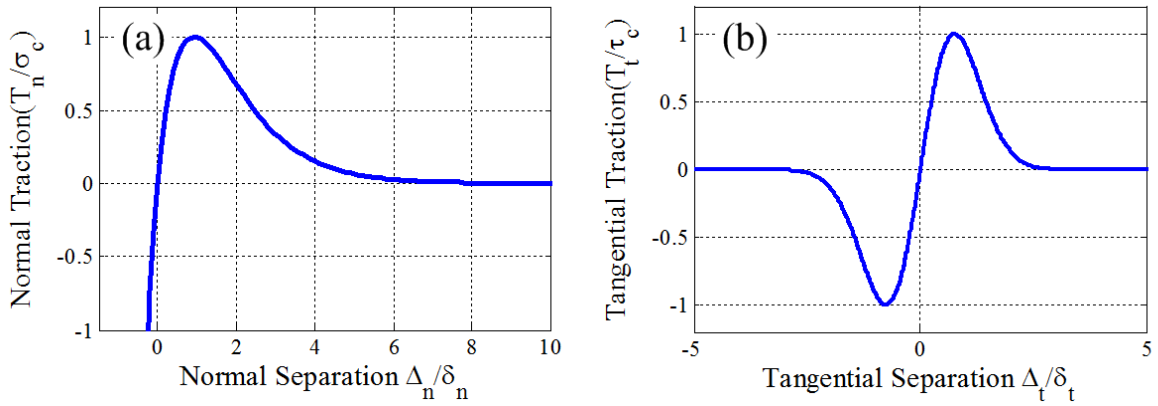

Fig. 1. (a) Uncoupled normal traction with the maximum tractionT_n^* at$\frac{\Delta_n}{\delta_n} = 1$; (b) Uncoupled shear traction with the maximum tractionT_t^* at$\frac{\Delta_t}{\delta_t} = \frac{1}{\sqrt{2}}$

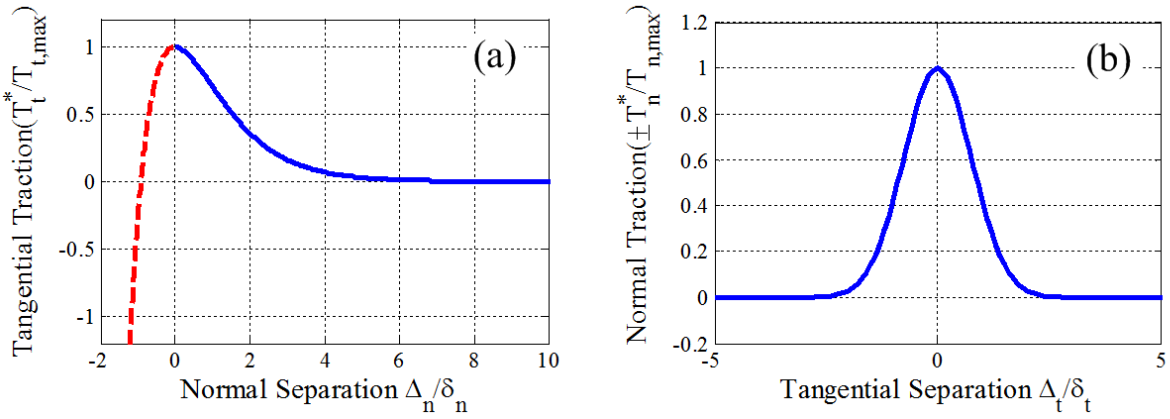

Fig. 2. (a)The maximum shear traction as a function of normal separation; (b)The maximum normal traction as a function of tangential separation.

The exponential traction-separation model has four independent parameters ($\varphi_n, \varphi_t, \sigma_c/\delta_n$ *and* τ_c/δ_t) and there is a coupling in the normal and tangential directions. The connections among those independent parameters will lead to unrealistic results. As shown in Fig. 2(a), the evolution of the maximum shear traction $T_t^*$is illustrated as a function of the normal separation. It can be seen that the maximum shear traction T_t^*will decrease to zero for increasing normal separations. However, the maximum shear traction T_t^* starts to decrease and even become negative when interface is under a large normal compression condition. This situation may lead to unrealistic results for interface under compressioncondition. In addition, when the interface is under compression, the maximum normal repulsive traction$-T_n^*$ will decrease to zero with the increasing of shear separation, see Fig. 2(b), and it might result in surface penetration.

3. The development ofanimproved interfacial bonding model

A potential function usually has a minimum at the equilibrium position in that the interaction force(derivative of the potential) must be attractive when distanceis larger than equilibrium position and repulsive when distance is smaller than equilibrium position.To overcome the limitations of the original exponential cohesive zone model[7], the following interface potential function is proposed with four additional variables c_1, c_2, δ_0 and Q:

$$\varphi(\Delta) = \varphi_0 \exp\left(-c_2 \frac{\Delta_n-\delta_0}{\delta_n-\delta_0}\right)\left\{\left[1+\frac{\Delta_n-\delta_0}{\delta_n-\delta_0}\right](Q-1) - Q\left[1+c_1\frac{\Delta_n-\delta_0}{\delta_n-\delta_0}\right] exp\left(-\frac{\Delta_t^2}{\delta_t^2}\right)\right\} \quad (5)$$

hereδ_0 represents the equilibrium position; the control variablesc_1, c_2 and Q aredetermined by the mixed-modedebonding boundary conditions; c_1, c_2 are used to overcome the unrealistic problem of original exponential cohesive zone model, that is, maximum shear traction T_t^* will decrease to zero when interface is under a large normal compression condition; $Q$is used to prevent surface penetration when interface is in compression; δ_n is the normal characteristicdebonding distance; δ_t is the tangential characteristic sliding distance; $\Delta_n = \mathbf{n}\cdot\Delta$ and $\Delta_t = \mathbf{t}\cdot\Delta$; $\mathbf{n}$ and $\mathbf{t}$ are the normal and tangential unit vectors on an element surface, respectively.

Differentiating Eq.(5) with respect to Δ_n and Δ_t yields the tractions in normal and tangential directions as:

$$T_n = \frac{\partial\varphi}{\partial\Delta_n} = \frac{\varphi_n}{\delta_n-\delta_0} exp\left(-c_{n2}\frac{\Delta_n-\delta_0}{\delta_n-\delta_0}\right)\left\{\frac{c_{n2}(1-Q_n)(\Delta_n-\delta_0)}{\delta_n-\delta_0} + (Q_n-1)(1-c_{n2}) + \left[(c_{n2}-c_{n1})Q_n + c_{n1}c_{n2}Q_n\left(\frac{\Delta_n-\delta_0}{\delta_n-\delta_0}\right)\right] exp\left(-\frac{\Delta_t^2}{\delta_t^2}\right)\right\} \quad (6)$$

$$T_t = \frac{\partial\varphi}{\partial\Delta_t} = \frac{2\varphi_t}{\delta_t}\left\{\left(\frac{\Delta_t}{\delta_t}\right)\left\{Q_t + c_{s1}Q_t\frac{\Delta_n-\delta_0}{\delta_n-\delta_0}\right\} exp\left(-c_{s2}\frac{\Delta_n-\delta_0}{\delta_n-\delta_0}\right) ex\,p\left(-\frac{\Delta_t^2}{\delta_t^2}\right)\right\} \quad (7)$$

whereφ_n is the normal fracture energy and φ_t is the shear fracture energy, which will be calibratedby different materials. The δ_0 in the normal traction-separation law is used to describe the interface thickness. So, when deriving the traction-separation laws, c_1, c_2, Qwere converted into c_{n1}, c_{n2}, $Q_n$in normal traction-separation law and converted intoc_{s1}, c_{s2}, $Q_t$in shear traction-separation law.In the proposed interfacial bonding model, the following fracture boundary conditions have to be satisfied for mixed-modefracture:

- The opening and sliding fracture energy are defined as:

$$\varphi_n = \int_{\delta_0}^{+\infty} T_n(\Delta_n, 0) d\Delta_n \,,\ \varphi_t = \int_0^{\infty} T_t(\delta_0, \Delta_t) d\Delta_t \quad (8)$$

- Normal and shear fracture energy are minimum at equilibrium position$(\delta_0, 0)$

$$\left.\frac{\partial \varphi}{\partial \Delta_n}\right|_{\Delta_n=\delta_0,\, \Delta_t=0} = 0,\ \left.\frac{\partial \varphi}{\partial \Delta_t}\right|_{\Delta_n=\delta_0,\ \Delta_t=0} = 0 \quad (9)$$

- Normal traction goes to zero$(T_n = 0)$when normal or tangential separation reaches the complete separation

$$T_n(+\infty, \Delta_t) = 0,\ T_n(+\Delta_n, \infty) = 0 \quad (10)$$

- Shear traction goes to zero$(T_t = 0)$when tangential or normal separation reaches the complete separation

$$T_t(\Delta_n, \infty) = 0,\ T_t(+\infty, \Delta_t) = 0 \quad (11)$$

- Normal and shear traction reach maximum when the separations reach the critical opening displacements$(\delta_n, \frac{\sqrt{2}}{2}\delta_t)$

$$\left.\frac{\partial T_n}{\partial \Delta_n}\right|_{\Delta_n=\delta_n, \Delta_t=0} = 0,\ \left.\frac{\partial T_t}{\partial \Delta_t}\right|_{\Delta_n=\delta_0, \Delta_t=\frac{\sqrt{2}}{2}\delta_t} = 0 \quad (12)$$

$$T_n(\delta_n, 0) = T_n^*,\ T_t\left(\delta_0, \frac{\sqrt{2}}{2}\delta_t\right) = T_t^* \quad (13)$$

- Shear traction will keep constant or increase when interface is in compression

$$T_t(\Delta_{n1}, \delta_t)|_{\Delta_{n1}<\delta_0} \geq T_t(\Delta_{n2}, \delta_t)|_{\Delta_{n2}<\delta_0} \quad under\ condition\ \Delta_{n1} < \Delta_{n2} \quad (14)$$

- Repulsive normal traction will not go to zero when two surfaces are still in contact

$$|T_n(\Delta_n, \Delta_t)|_{\Delta_n<\delta_0,\, \delta_t<\Delta_t\ll\infty} > 0 \quad (15)$$

From Eqs.(8)-(9), we have the normal energy $\varphi_n = exp(1)\,\sigma_c(\delta_n - \delta_0)$, which requires $c_{n1} = c_{n2} = 1$, we have the shear energy$\varphi_t = \sqrt{\frac{\exp(1)}{2}}\tau_c\delta_t$, which requires $Q_t = 1$ .The σ_c is the normal strength, which can be used to define different interfacial strength in normal direction. Theτ_c is the shear strength, which can be used to describe different interfacial strength in shear direction. To satisfy Eqs.(10)-(11), additional conditions($c_{s1} = 0\,, c_{s2} > 0\ and\ Q_n = 1$)are required. Then, Eqs.(12)-(13) will be automatically satisfied, which means when the interface is in tension, it requires $c_{n1} = c_{n2} = 1, c_{s1} = 0\,, c_{s2} > 0\ and\ Q_n = 1$. When the interface is in compression, it requires $c_{s1} = 0\ and\ c_{s2} \geq 0$ to satisfy Eq.(14). In normal direction, it is necessary to set$0 < Q_n < 1$to satisfy Eq.(15)to prevent surface penetration.

It is worth mentioning that when $c_{n1} = c_{n2} = c_{s1} = c_{s2} = Q_t = Q_n = 1\ and\ \delta_0 = 0$, the proposed model can be reduced to the improved exponential cohesive zone model [20].

The Fig.3 plots the normal and tangential traction-separation laws from the proposed model. The variation of normal traction T_n as a function of Δ_n across the interface under the condition of $\Delta_t = 0$ is graphically shown in Fig.3(a). The value of T_n will increase with increasing normal separation until reaching maximum normal traction T_n^*. After the maximum normal traction T_n^* has been reached, the normal traction gradually decreases to zero. Fig.3(b) illustrates the variation of shear traction T_t expressed in terms of Δ_t under the condition $\Delta_n = \delta_0$.

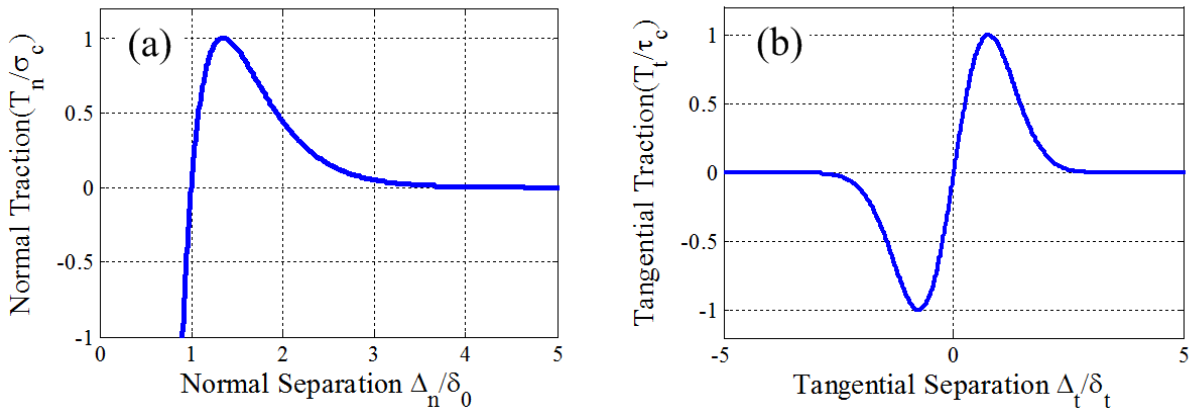

Fig.3. Interfacialtraction variation with separation: (a) Uncoupled normal traction; (b)Uncoupled shear traction.

To overcome the unrealistic problem of original exponential cohesive zone model, the control variablec_{s1}, c_{s2} was introduced in the shear traction-separation law. When the interface is in tension, by setting $c_{s1} = 0, c_{s2} = 1$, it can be seen that the maximum normal traction T_t^* will decrease to zero as the normal separation increases, as shown in Fig.4 (a) (the red line). When the interface is in compression, by setting $c_{s1} = 0, c_{s2} = 1$, the maximum shear traction T_t^* increases as the normal separation decreases (c.f. Fig.4(a) black line),if $c_{s1} = 0, c_{s2} = 0$, the maximum shear traction T_t^*will keep constant (c.f. Fig.4(a) blue line). In fact, $c_{s1}\ and\ c_{s2}$ can be tuned to regulate the relation between the maximum shear traction T_t^* and the normal separation Δ_n when interface is in compression.

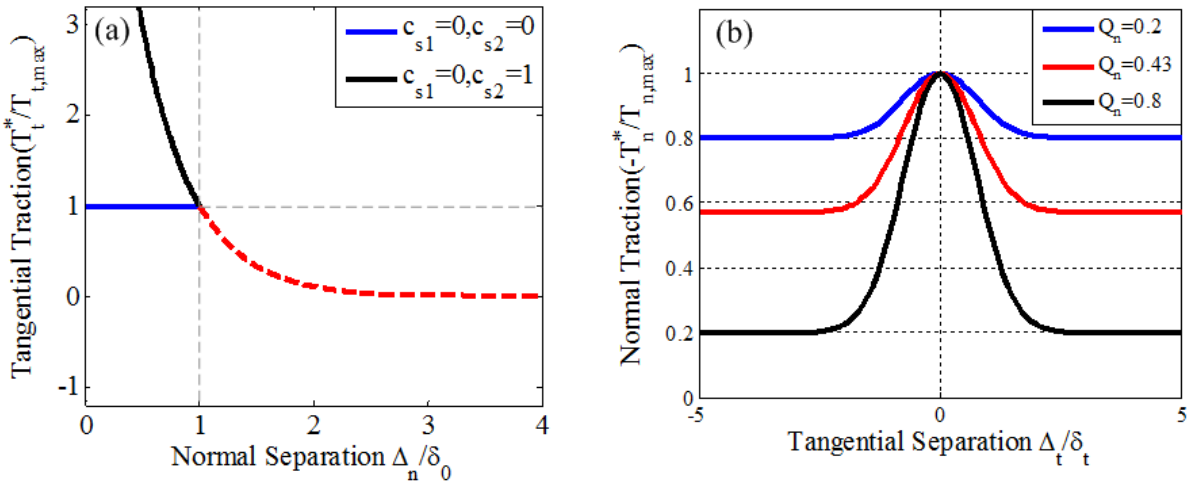

Fig.4. Compressive condition: (a) The maximum shear traction T_t^* as a function of normal separation in compression; (b) The maximum normal repulsive traction $-T_n^*$ as a function of tangential separation.

From Xu and Needleman's exponential model, when interface is in tension, it is reasonable to have the maximum normal traction T_n^* diminish as the tangential separation reaches to the limit as shown in Fig. 2(a). However, when the interface is in compression, the maximum normal traction T_n^* will decrease to zero, thus resulting in the zero resistant to normal deformation and subsequently allowing for surface penetrations. To solve this problem, one method is to degrade the normal traction-separation law to pure contact condition. In the meanwhile, the compressive stiffness was increased by 10 times to prevent surface penetration [30]. The other method is to enforce contact algorithm in the contact surface [31]. In our model, we simply set the value of Q_n in the range of $0 < Q_n < 1$ when interface is in compression to fix the penetration problem.As illustrated in Fig.4(b), the maximum normal repulsive traction $-T_n^*$ will not decrease to zero at the condition of large tangential separation.The smaller the value of Q_n, the larger the normal traction between the two contact surfaces. Through a parametric study, we found out $Q_n = 0.43$ works very well in our simulation to handle the penetration problem. Thus, the model has the capability to sustain compressive deformation without special treatment or enforcing a contact algorithm.

4.Path dependence of work-of-separation

The amount of energy dissipated strongly depends on separation paths when the normal and shear fracture energy in the interfacial zone are different.To evaluate the energy variation with

respect to separation path, it is necessary to study the work-of-separation[20]. Many experimental data illustrates that the work-of-separation in normal direction is not equal tothe work in tangential direction,e.g. Araki et al. [14], Benzeggagh and Kenane[15], Dollhofer et al. [16], Pang [17], Warrior et al. [18] and Yang et al. [19]. Therefore, the work-of-separation under combined normal and shear loading is analyzed with unequal normal and shear energy to study the influence of coupling parameters of the proposed interfacial bonding model.

4.1. Non-proportional separation

In the first case, the interfacial zone is loaded in normal direction up to a maximum displacement of $\Delta_{n,max}$ with $\Delta_t = 0$. Then, the normal displacement is kept at this maximum point and subsequently the shear loading is applied until completelyseparation in shear direction($\Delta_t \to \infty$). The normal work-of-separation, the tangential work-of-separation and the total work is calculated as[10, 20]:

$$W_{tot} = W_n + W_t = \int_{\delta_0}^{\Delta_{n,max}} T_n(\Delta_n)\Big|_{\Delta_t=0} d\Delta_n + \int_0^{\infty} T_t(\Delta_t)\Big|_{\Delta_n=\Delta_{n,max}} d\Delta_t \qquad (16)$$

In the second case, the interfacial zone is loaded in tangential direction up to a maximum displacement of $\Delta_{t,max}$ with $\Delta_n = \delta_0$. Subsequently, the shear displacement is kept at this maximum point and thenloading in normal direction is applied until completely separation($\Delta_n \to +\infty$). The tangential work-of-separation,the normal work-of-separation and the total work is calculated as[10, 20]:

$$W_{tot} = W_t + W_n = \int_0^{\Delta_{t,max}} T_t(\Delta_t)\Big|_{\Delta_n=\delta_0} d\Delta_t + \int_{\delta_0}^{+\infty} T_n(\Delta_n)\Big|_{\Delta_t=\Delta_{t,max}} d\Delta_n \qquad (17)$$

As shown in Fig. 5(a) and Fig. 6(a), the total work equals the shear work ($W_{tot} = W_t$) when $\Delta_{n,ma} = \delta_0$ and the total work equals the normal work ($W_{tot} = W_n$) when $\Delta_{t,max} = 0$. Furthermore, the total work varies very smoothly from shear work to normal work (Fig. 5(a) and Fig. 6(a)) or from normal work to shear work (Fig. 5(b) and Fig. 6(b)). The curves of work-of-separation clearly illustrate the realistic changes of work under mixed-mode loading.

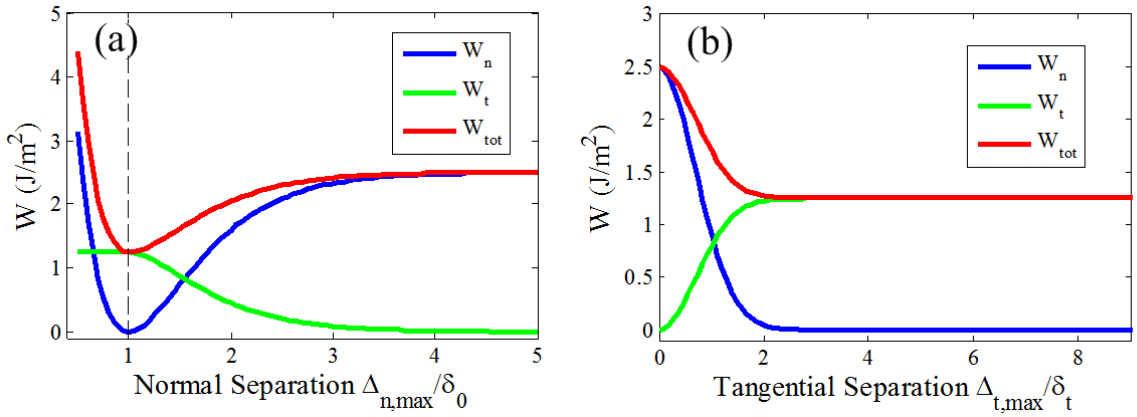

Fig. 5. ($c_{s2} = 0$ *with interface under compression*, $\varphi_n = 2.5\text{J}/m^2, \varphi_t = 1.25\text{J}/m^2$): (a) Work-of-separation vs. $\Delta_{n,max}$; (b) Work-of-separation vs. $\Delta_{t,max}$

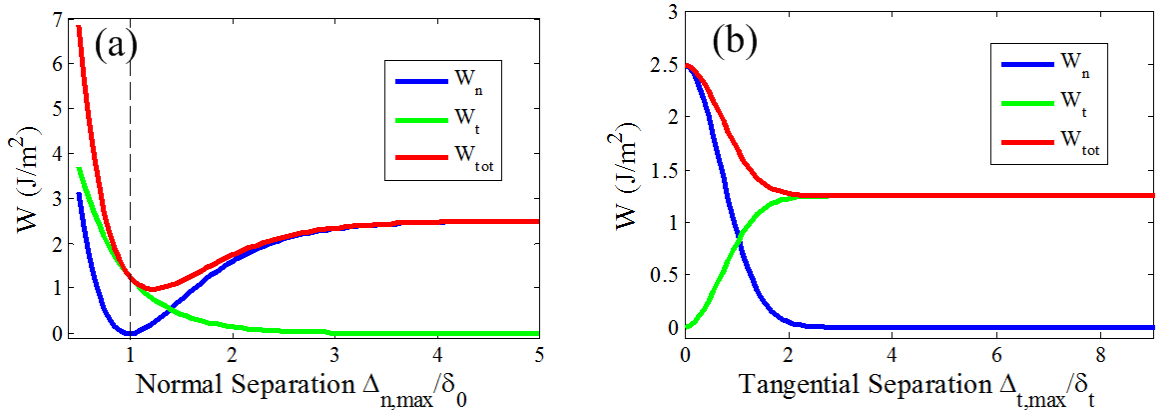

Fig. 6. ($c_{s2} = 1$ *with interface under compression*, $\varphi_n = 2.5\text{J}/m^2, \varphi_t = 1.25\text{J}/m^2$):(a)Work-of-separation vs. $\Delta_{n,max}$;(b)Work-of-separation vs. $\Delta_{t,max}$

4.2. Proportional separation

The proportional separation path is associated with the separation angle(α), which is a realistic coupling separation in both normal and tangential directions. The work-of-separation of proportional separation for the proposed interfacial bonding model is defined as[10]:

$$W_{tot} = W_n + W_t = \int_{\delta_0}^{+\infty} T_n(\Delta sin\alpha, \Delta cos\alpha) sin\alpha d\Delta_n + \int_0^{\infty} T_t(\Delta sin\alpha, \Delta cos\alpha) cos\alpha d\Delta_t \quad (18)$$

where$\Delta = \sqrt{(\Delta_n - \delta_0)^2 + \Delta_t^2}$ and $\delta = \sqrt{(\delta_n - \delta_0)^2 + \delta_t^2}$.

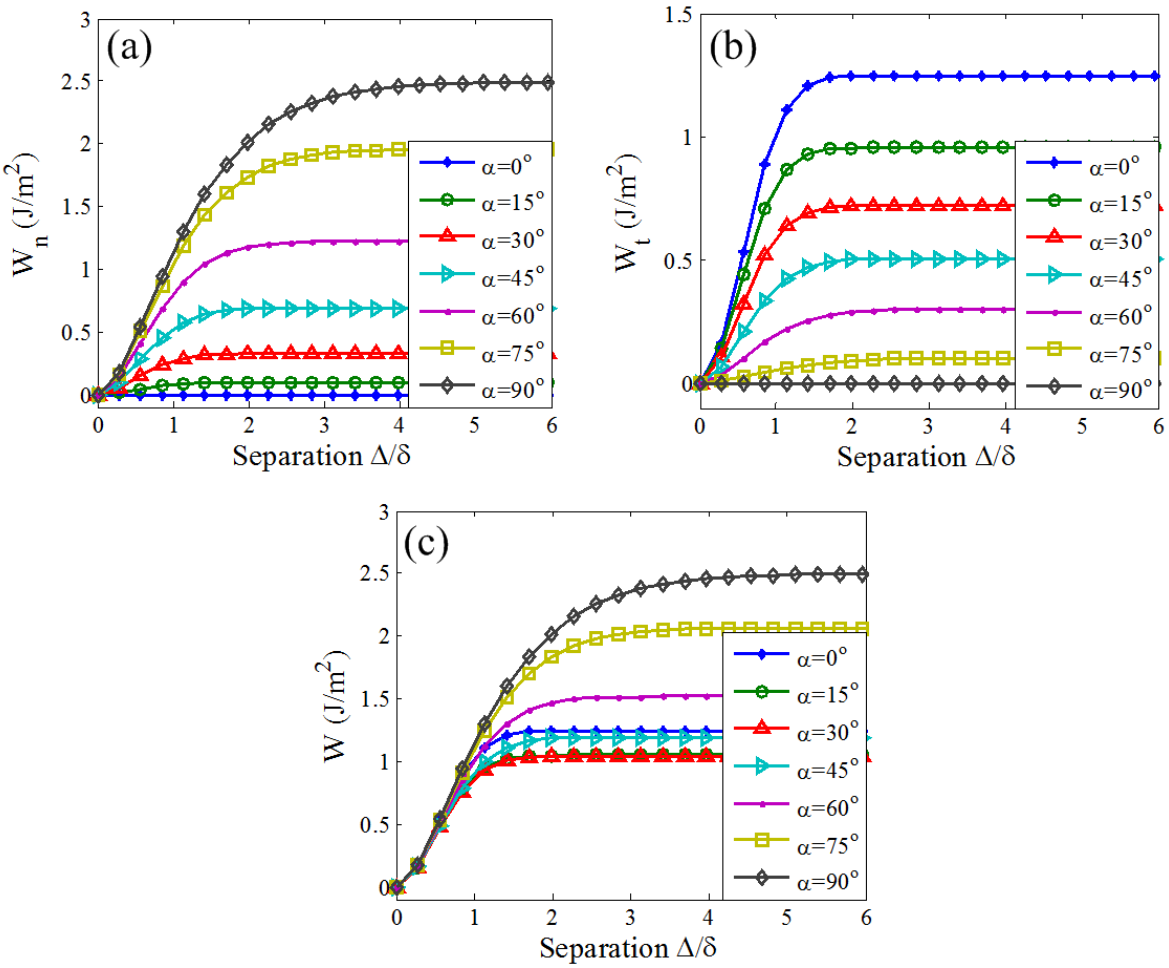

Fig.7. The proportion separation of the proposed interfacial bonding model ($\varphi_n = 2.50\mathrm{J}/m^2, \varphi_t = 1.25\mathrm{J}/m^2$): (a)Work-of-separation in normal direction; (b) Work-of-separation in tangential direction; (c) Total work-of-separation

When the debonding process is along 90° (normal direction), the work-of-separation is pure mode I and it equals normal energy ($W_{tot} = W_n$). The work-of-separation is pure mode II during the debonding process when $\alpha = 0°$ and it equals shear energy ($W_{tot} = W_t$). One would expect that the work-of-separation is in mixed-mode decohesive process when the debonding angle is between 0° *and* 90°. The work-of-separation for proportional separation is illustrated in Fig.7. From Fig.7(a), it can be seen that the work-of-separation in normal direction is decreasing when the debonding angle is decreasing. The work-of-separation in shear direction is increasing as the decohesive angle α decreasing, as shown in Fig.7(b). The Fig.7(c) illustrates the total work-of-separation ($W_{tot} = W_n + W_t$) during mixed-mode decohesion.

5. Model Verification

5.1. Analytical analysis

The proposed interfacial bonding model was verified through analytical solutionwhen the interface is inlinear elastic deformation. Theanalytical solution of stress-strain relation is derived based on a simple compression test in a standard hexagonal structure, as shown in Fig. 8.Thehexagonal plates will slide each other along the interface duringcompressive loading process. The red springs between bulks in Fig. 8(a) represent the interface traction.

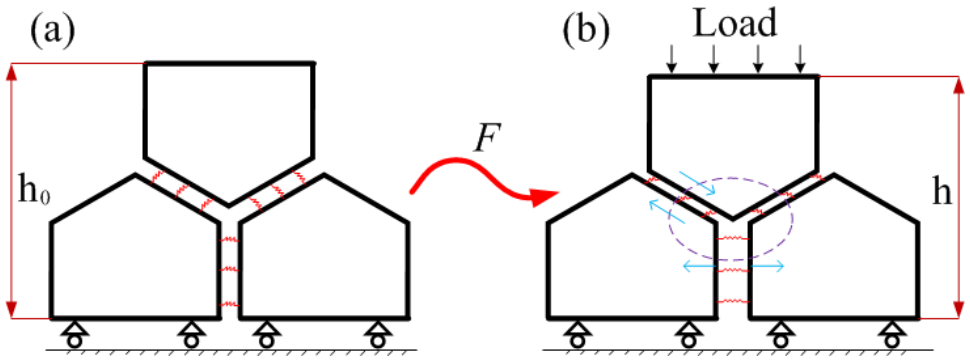

Fig. 8. Compression test:(a)Original configuration;(b)Deformed configuration

From the deformed configuration in Fig. 8(b) and Fig. 9, the force equilibrium and compatibility equations can be obtained. In Fig. 9 (b), the black dash line denotes the original hexagonal surface and red solid line represents the current hexagonal surface. The parameters used in the derivation of the analytical solution are defined in Fig. 9(b)-(c).

According to Fig. 9, the stress(σ_b)-strain(ε_b) relation can be obtained as (c.f. Appendix A):

$$\sigma_b = E_n\left(\frac{h_0\varepsilon_b}{t_0 cos\theta} - \frac{\sqrt{4t_0^2-2\sqrt{3}t_0(t_0 cos\theta - h_0\varepsilon_b)}-t_0}{\sqrt{3}t_0}tan\theta\right) + G_s\frac{\sqrt{4t_0^2-2\sqrt{3}t_0(t_0 cos\theta - h_0\varepsilon_b)}-t_0}{\sqrt{3}t_0}tan\theta \qquad (19)$$

Where σ_b is the bulk stress; $\varepsilon_b$is applied strain; E_n represents the modulus of interface in normal direction;G_s is the shear modulus of interface;t_0 is the original interface thickness; θ is the geometry angle of hexagon; h_0 is the original height of the hexagonal structure. Detailed derivation of analytical solution for the stress-strain relation can be found in Appendix A.

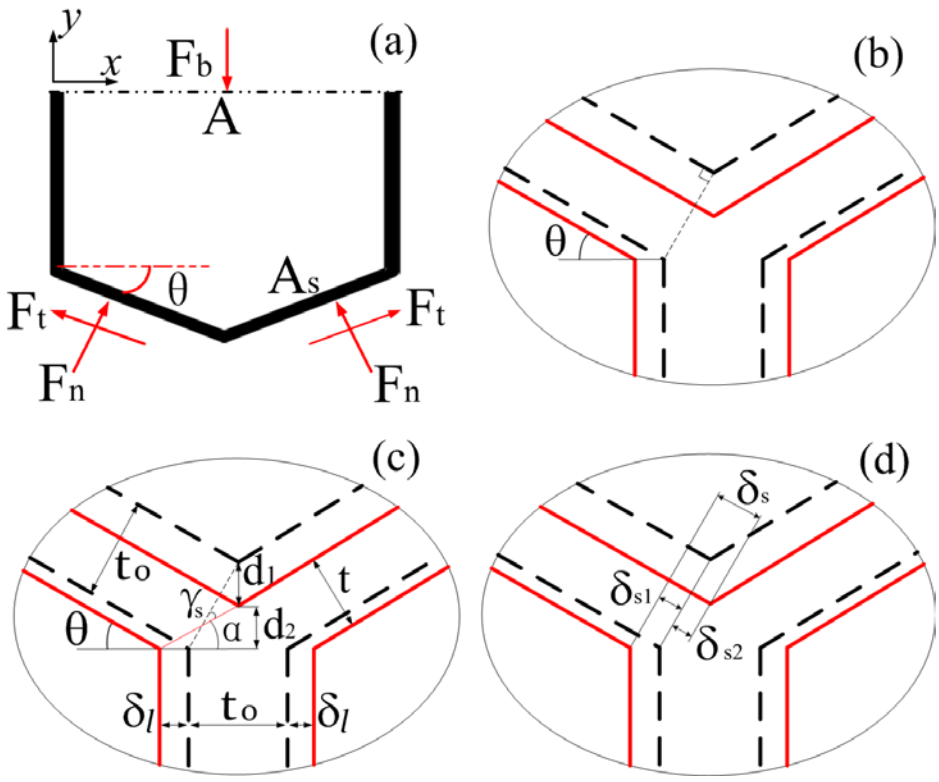

Fig. 9. Analytical model:(a) Force equilibrium; (b)Compatibility relationship (zoom in view from Fig. 8(b) dash elliptical region); (c-d) Details ofparameters used in analytical solution.

5.2.Finite Element Implementation

Following standard procedures and neglecting the body force, a Galerkin weak formulation can be expressed as following:

$$\int_{\Omega} \mathbf{P}: \delta\mathbf{F} d\Omega - \int_{S_{inter}} \mathbf{T}^{inter} \cdot \delta\Delta dS = \int_{S_{ext}} \overline{\mathbf{T}} \cdot \delta\mathbf{u} dS - \int_{\Omega} \rho\ddot{\mathbf{u}} \cdot \delta\mathbf{u} d\Omega \qquad (20)$$

where**P** is the first Piola-Kirchhoff stress tensor;**F** is the deformation gradient;Δ denotes the interface displacement jump across the interfaces; Ω, S_{inter} , S_{ext} are the volume, internal interface boundary and external traction boundary of element in the reference configuration;ρ represents the material density in the reference configuration, $\overline{\mathbf{T}}$denotes the external traction vector and $\mathbf{T}^{inter}$ is the interfacialbonding traction vector. The explicit time integration scheme is applied, which is based on the Newmarkβ method with $\beta = 0$ and $\gamma = 0.5$[32].

5.3.Simulation Results vs. Analytical Solutions

Numerical simulations have been carried out for the same specimen as in the analytical analysis. The exact problem statement is shown in Fig. 10, and the length of hexagon edge is $15nm$. Thus, the specimen width is $L_x = 25.98nm$, and length is $L_y = 39.232nm$. The specimen is under compressive loading along y direction and the bottom is set as roller boundary condition as shown in Fig. 10.

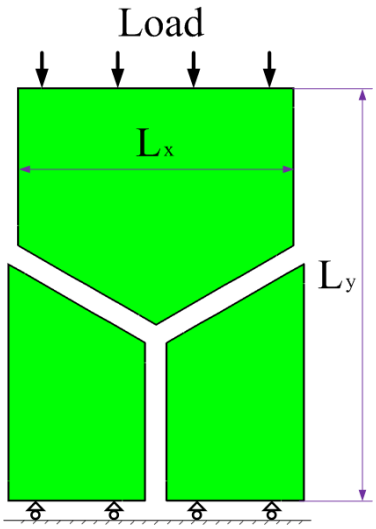

Fig. 10. Simulation specimen and problem setup for a simple case

In the simulation, the material properties for the bulk constituents were chosen as: Young's modulus $E = 100\text{GPa}$, Poisson's ratio $v = 0.28$ [33], mass density $\rho = 3190kg/m^3$ [34] and the interfacial zone properties are $\sigma_c = \tau_c = 55\text{MPa}$ and $\varphi_n = 0.052J/m^2, \varphi_t = 0.032J/m^2$ [35]. The initial interfacial zone thickness is $t_0 = \delta_0 = 2nm$. In this case, when the interface is in tension, the parameters are taken as $c_{n1} = c_{n2} = c_{s2} = Q_t = Q_n = 1 \; and \; c_{s1} = 0$, and when the interface is in compression, we set $Q_n = 0.43 \; and \; c_{s1} = c_{s2} = 0$. The deformation and stress distribution of the specimen is shown in Fig. 11 at different loading strain ε_b.

Based on the interface geometry parameters and material properties used in our numerical simulation, we can easily obtain the stress-strain relation from the analytical solution (Eq.19). The stress-strain relation of simulation results and analytical solutions was illustrated in Fig. 12.

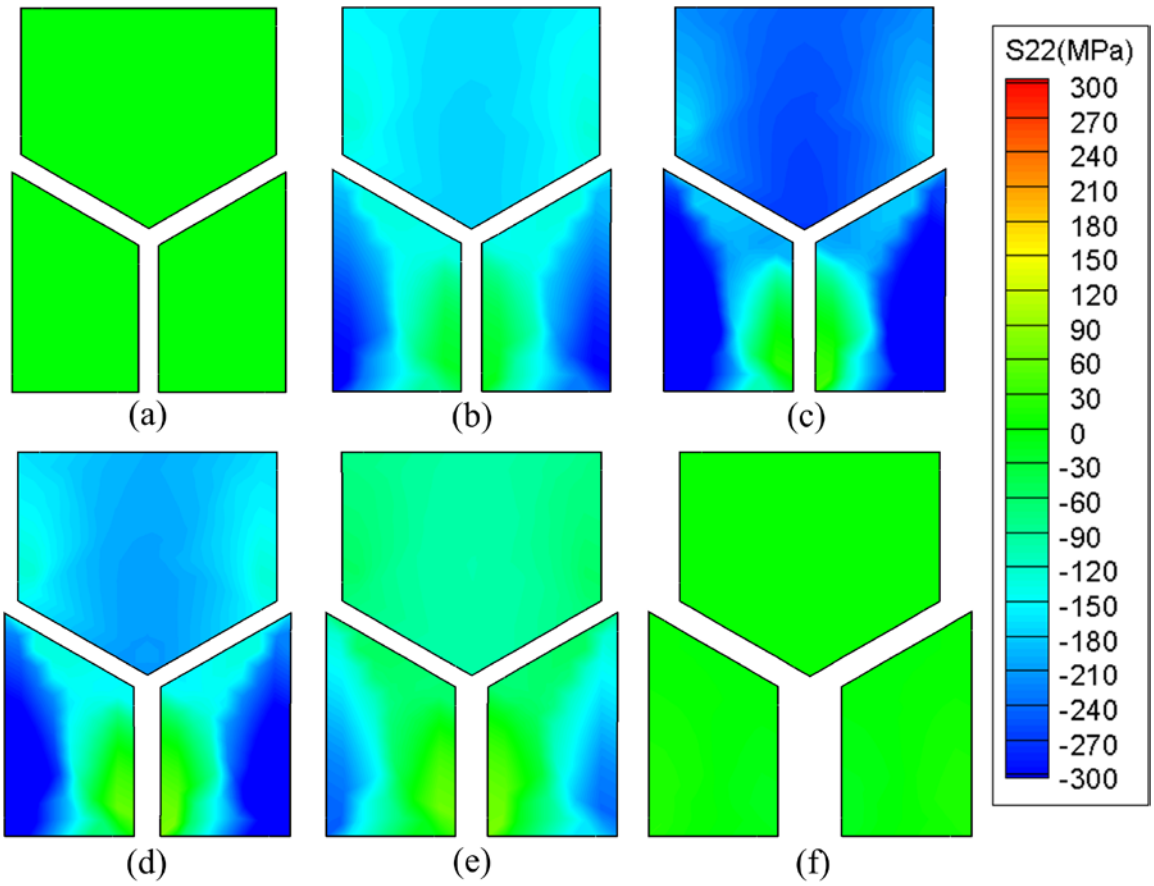

Fig. 11. Snapshot of stress distribution(σ_{22}) at different loading strain: (a)$\varepsilon_b = 0\%$; (b)$\varepsilon_b = 0.8\%$; (c)$\varepsilon_b = 1.3\%$; (d)$\varepsilon_b = 1.5\%$; (e)$\varepsilon_b = 1.6\%$; (f)$\varepsilon_b = 1.8\%$

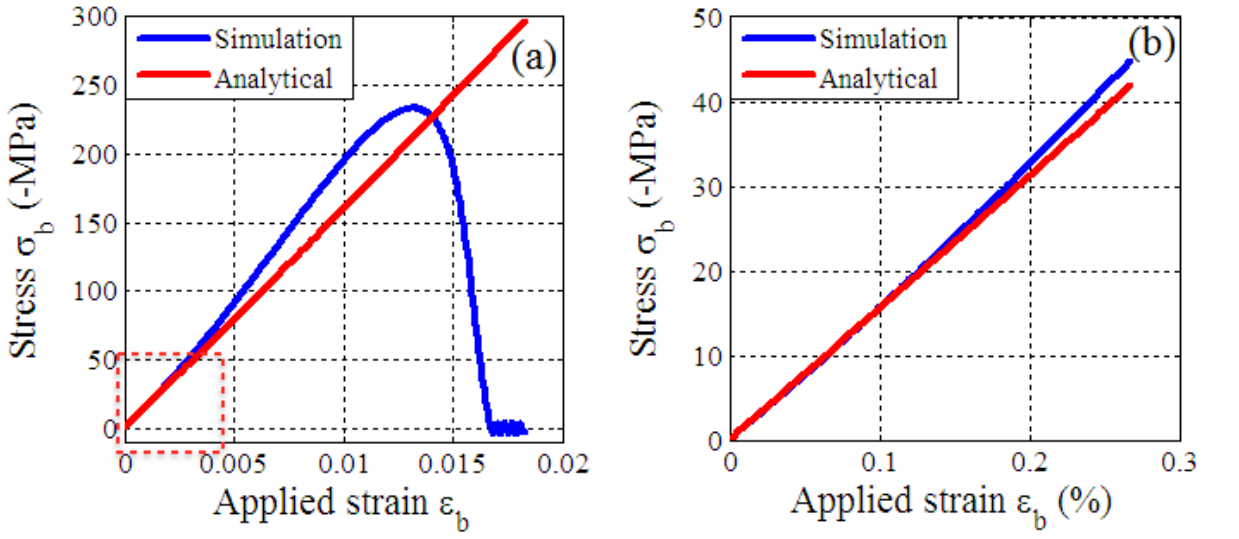

Fig. 12. Comparison between the analytical solutions and the numerical simulation results($\sigma_b - \varepsilon_b$):(a) the whole region; (b) linear elastic region

Due to the small-angle approximation in analytical solution derivation, we only compared the simulation results and analytical solution within 0.3% strain in this case. As strain increases, the accumulation error will increase as shown in Fig. 12. The major reason for the differences between the numerical results and analytical solution is that the linear elastic small deformation is assumed in the derivation of the analytical solution; however the exponential traction-separation law is used to govern the interfacial interaction in numerical simulation. It can be seen that the stress-strain curve of simulation results was consistent with the curve of analytical solutions in small linear elastic deformation region. Nonetheless, we should say that the model developed in this work is not only for fracture simulation, it canbe also usedto model cell-cell/substrate interactions.Soit is meaningful to compare with analytical solution for linear elastic deformation at the interface. In addition, we have compared our model with experimental data for bone fracture simulation in Section 6, which is inelastic.

6. Numerical simulationof extrafibrillar matrix in bone

Studying the fracture mechanism in bone is attracting the attention of engineering researchers, due to its highly hierarchical structure and the exceptional mechanical and load-bearing properties, e.g. Rho et al. [36],Weiner and Wagner [37] and Weiner et al.[38]. Bone poses various levels of hierarchical structural organization from macroscale to nanoscale[36, 39]. The mechanism of bone failure has been extensively studied, however, the underlying mechanism of plastic deformation in bone is still a debating issue. The possible pathways for plastic flow in bone are most likely due to the sliding between mineral crystals[40], between mineral and collagen phases[40], or between the mineralized collagen fibrils[41-43].

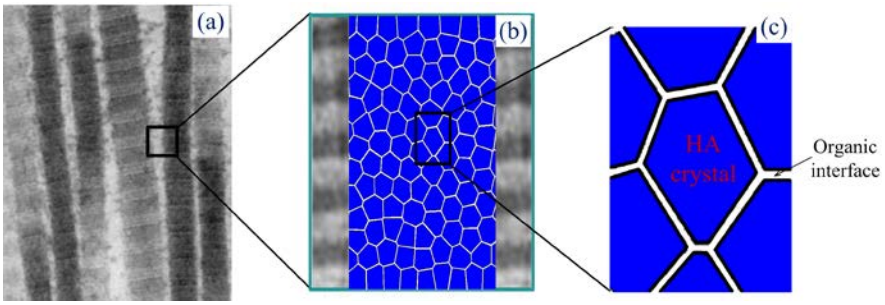

Fig.13. Schematic representation of ultrastructure of extrafibrillar matrix:(a) extrafibrillar matrix;(b)HA crystals in extrafibrillar matrix; (c) Organic interface between HA crystals.

At ultrascale level, the extrafibrillar matrix in bone consists of hydroxyapatite (HA) polycrystals bounded through an organic interface (grain boundary), as shown in Fig.13. This organic interface consists of a group of non-collagenous proteins, such as osteocalcin, osteopontin and proteoglycans [44]. To explore the bulk mechanical properties of bone materials, it is important to understand the mechanical response of its microstructure.

For simplicity while ensuring reasonable accuracy, a 2D plane strain model of granular HA crystals bounded through a thin interface was proposed to mimic the microstructure of extrafibrillar matrix in bone. The geometry of the specimen was generated by Voronoi tessellation method, e.g.Du et al. [45] and Lin et al. [46]. The exact problem statement is shown in Fig. 14, in which a 2D plate with dimension ($L_x \times L_y = 322nm \times 322nm$) is under compressive loading in y axis. In this simulation, there are 144 grain cells and the average grain size is around $25nm$[47-49].The thickness of organic interface was set to be $t_0 = \delta_0 = 2\text{nm}$ throughout the model, which was estimated based on the volume ratio of organic interface (~ 10% by volume) and the average grain size (~25nm) in the extrafibrillar matrix[50, 51].

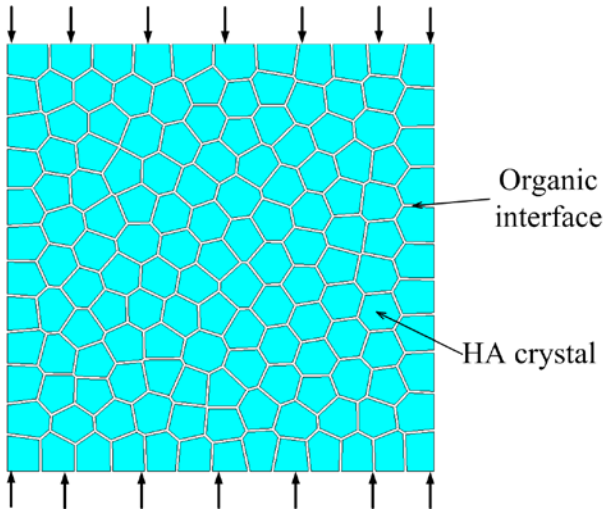

Fig. 14. Simulation problem set up of extrafibirllar matrixstructure

The organic-inorganic interface in extrafibrillar matrix may contain different chemical bonds and the environments are truly complicated. A direct experimental measurement of interface properties and behaviors for extrafibrillar matrix is very challenging. In the current work, the thickness of organic interface is assumed to be around 2nm and comprised of a monolayer of molecules. Under this assumption, the interface would behave like an interfacial molecular bond between the hydroxyapatite grains, thus making the proposed cohesive zone law suitable for this

case. The interfacial interaction was assumed as intermediate type of interfacial bonds (hydrogen bonds).The material properties for the bulk constituents were chosen as: Young's modulus $E = 100\text{GPa}$, Poisson's ratio $v = 0.28$ [33], mass density $\rho = 3190kg/m^3$ [34] and the proposed interfacial zone properties wereset as $\sigma_c = \tau_c = 55\text{MPa}$ and $\varphi_n = 0.052J/m^2, \varphi_t = 0.032J/m^2$[35]. In this case, when the interface was under tension, the parameters were taken as $c_{n1} = c_{n2} = c_{s2} = Q_t = Q_n = 1\ and\ c_{s1} = 0$, and when the interface was under compression, we set $Q_n = 0.43\ and\ c_{s1} = c_{s2} = 0$.

In this work, all simulations were implemented using a custom-developed finite element package [23, 52-55].We first performed the mesh refinement studies and found out that the maximum stress in the specimen was decreasing as mesh number increasing (mesh size decreasing) and the stress would reach a convergent value when the mesh size is below 7.5nm as shown in Fig. 15.

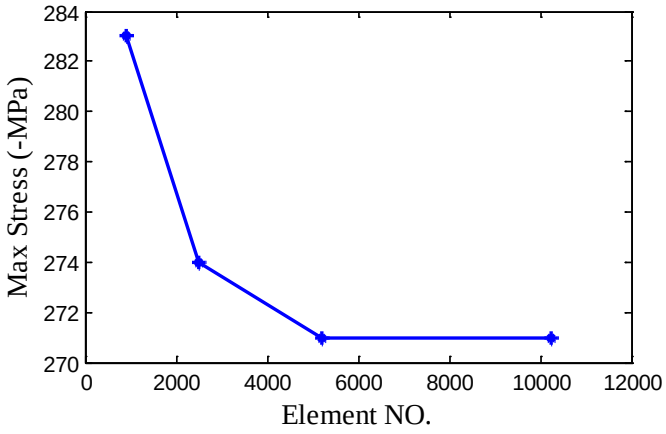

Fig. 15. Mesh convergence test

After the mesh convergence test, we have run six simulation cases with random polycrystalline grain distribution. The deformation process from one of the simulation cases was shown in Fig. 16. The stress distribution along loading direction was captured from the simulation. From this study, we measured the averaged crack path and it was along an inclined angle($\approx 33°$), which was very similar to the angle of cross-hatch cracks observed in bone compression test [56]. Furthermore, as shown in Fig. 17, the elastic modulus estimated from the simulation was around $15GPa$, which was in the range of nanoindentation modulus of bone reported in the literature [57, 58]. In addition, the estimated maximum value of the average mineral strain($\sim 0.24 \pm 0.03\%$) was consistent with the experimental studies($0.27 \pm 0.03\%$)[59, 60]. In Fig. 17, the error bars are the standard deviation. The simulation results indicated that this improved interfacial bonding

model could capture the sliding process along the interface between the HA crystals and the overall failure behavior of the extrafibrillar matrix in bone (see Fig. 16).

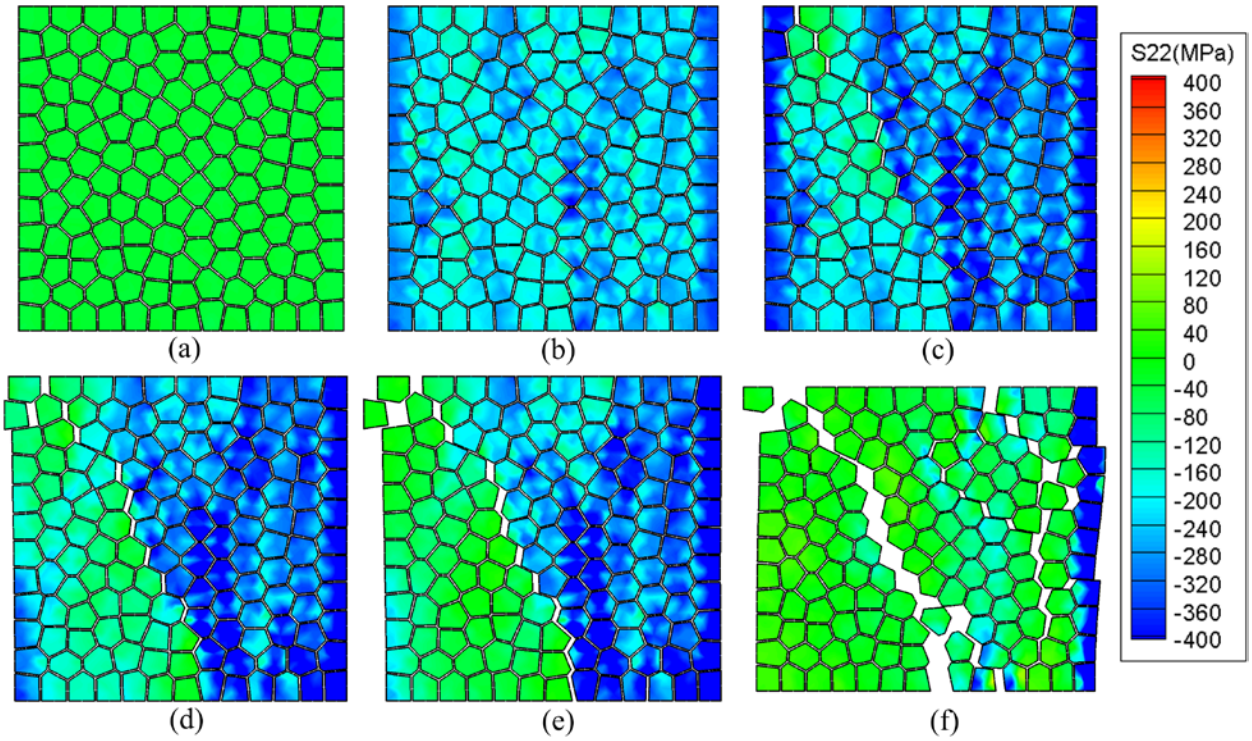

Fig. 16. Snapshot of stressdistribution(σ_{22}):(a)ε_b=0.30%;(b)ε_b=1.28%;(c)ε_b=1.52%;(d)ε_b=1.58%;(e)ε_b=1.64%;(f)ε_b=1.95%

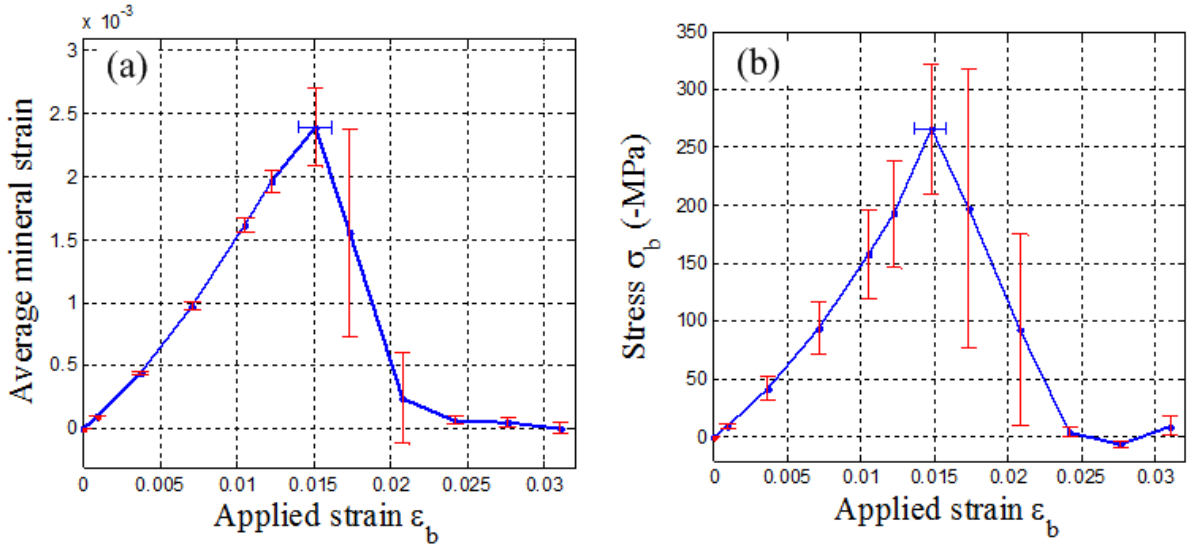

Fig. 17.(a)Average mineral strain vs.applied strain (ε_b); (b)Bulk stress(σ_b) vs.applied strain(ε_b)

7. Conclusions

In this work, we have reported animproved interfacialbonding model. The proposed model wasexamined in mixed-mode loading and the physically realistic coupling behavior was obtained. The work-of-separation analysis implies that the proposed interfacial bonding model can capture the work-of-separation in mixed mode, which is a realistic process for work transformation from normal to shear or from shear to normal. The proposed improved interfacial bonding model has the following properties:

(1) By introducing the equilibrium distance δ_0, our model characterizes both attractive and repulsive interfacial interactions and can be applied to model material interfaces under both tension and compression, while the traditional cohesive zone model may need anadditional treatment in the interface to avoid surface penetration when the interface surfaces are in compression.

(2) By assigning propervalues to the control variables($c_1, c_2 and\ Q$)in the normal and tangential traction-separation laws, the proposed interfacial zone model satisfied all fracture boundary conditions for mixed-mode fracture as indicated in Section 3.

(3) The proposed interfacial zone model does not require equal fracture energy in the normal and shear direction. The assumption that the normal fracture energy (φ_n)equals the shear fracture energy (φ_t)is often not consistent with experiment measurements.

(4) When interface is undercompression($\Delta_n < \delta_0$), the maximum shear traction (T_t^*)could either increase or keep constant as Δ_n decreasing, which appears to be realistic[61].

(5) The proposed interfacial zone model can be reduced to an improved exponential cohesive zone model [20] by assigning proper values to the control varablesand thus the proposed model preserves all essential features of an improved exponential cohesive zone model.

The proposed interfacial bonding model wasverified by analytical solution when the interface is in linear elastic deformation. The stress-strain ($\sigma_b - \varepsilon_b$) curve obtained from numerical simulation and analytical solution agreed well in linear elastic region as illustrated inFig. 12.By employing the generalized interfacial bonding model to theorganic interface modeling of extrafibrillar matrix in bone, the simulation results successfully captured the HA crystal sliding along the organic interface to form a damage zonein extrafibrillar matrix(c.f. Fig. 16). In addition, the inclined crack angle, elastic modulus and average maximum mineral strain obtained from

simulation (c.f. Fig. 17) wereconsistentwith experimental observations. Hence, through the interfacial modeling, the current research provides a numerical simulation tool to study the interface interactions in biological materials. Nonetheless, there are several limitations associated with the current study of extrafibrillar matrix behavior in bone. Firstly, crystal shape/size are estimated from the experimental observations[41, 49], so the Voronoi generated grains are appropriate representations of the extrafibrillar mineral crystals. However, the crystal size, orientation and aspect ratio effects were not studied in the current study and need further investigation since these factors may also play roles in dictating the extrafibrillar matrix mechanical properties. Secondly, the organic interface properties are simply estimated based on the experimental observations and related information reported in the literatures, which do not consider complex chemical bonding and environment of organic-inorganic interface and may be used only for qualitative analysis.

Acknowledgements

This work is partially supported by a grant from National Institutes of Health (Grant No. R21AR066925),a grant from National Science Foundation (Grant No. CMMI-1538448), and a grant from the University of Texas at San Antonio, Office of the Vice President for Research.We are grateful to Dr. Hai-Chao Han for valuable discussions in the derivation of the analytical solution.

References

[1] Barthelat F, Rabiei R. Toughness amplification in natural composites. J MechPhys Solids. 2011;59:829-40.
[2] Xiao S, Belytschko T. A bridging domain method for coupling continua with molecular dynamics. Computer Methods in Applied Mechanics and Engineering. 2004;193:1645-69.
[3] Curtin WA, Miller RE. Atomistic/continuum coupling in computational materials science. Modelling and Simulation in Materials Science and Engineering. 2003;11:R33.
[4] Miller R, Tadmor E, Phillips R, Ortiz M. Quasicontinuum simulation of fracture at the atomic scale. Modelling and Simulation in Materials Science and Engineering. 1998;6:607.
[5] Gao H, Klein P. Numerical simulation of crack growth in an isotropic solid with randomized internal cohesive bonds. Journal of the Mechanics and Physics of Solids. 1998;46:187-218.
[6] Tvergaard V, Hutchinson JW. The relation between crack growth resistance and fracture process parameters in elastic-plastic solids. J MechPhys Solids. 1992;40:1377-97.

[7] Xu X-P, Needleman A. Numerical simulations of fast crack growth in brittle solids. Journal of the Mechanics and Physics of Solids. 1994;42:1397-434.
[8] Camacho G, Ortiz M. Computational modelling of impact damage in brittle materials. International Journal of solids and structures. 1996;33:2899-938.
[9] Geubelle PH, Baylor JS. Impact-induced delamination of composites: a 2D simulation. Composites Part B: Engineering. 1998;29:589-602.
[10] Park K, Paulino GH, Roesler JR. A unified potential-based cohesive model of mixed-mode fracture. Journal of the Mechanics and Physics of Solids. 2009;57:891-908.
[11] Falk ML, Needleman A, Rice JR. A critical evaluation of cohesive zone models of dynamic fractur. Le Journal de Physique IV. 2001;11:Pr5-43-Pr5-50.
[12] Rahulkumar P, Jagota A, Bennison S, Saigal S. Cohesive element modeling of viscoelastic fracture: application to peel testing of polymers. International Journal of Solids and Structures. 2000;37:1873-97.
[13] Yuan H, Chen J. Computational analysis of thin coating layer failure using a cohesive model and gradient plasticity. Engineering Fracture Mechanics. 2003;70:1929-42.
[14] Araki W, Nemoto K, Adachi T, Yamaji A. Fracture toughness for mixed mode I/II of epoxy resin. Acta materialia. 2005;53:869-75.
[15] Benzeggagh M, Kenane M. Measurement of mixed-mode delamination fracture toughness of unidirectional glass/epoxy composites with mixed-mode bending apparatus. Composites Science and Technology. 1996;56:439-49.
[16] Dollhofer J, Beckert W, Lauke B, Schneider K. Fracture mechanical characterisation of mixed-mode toughness of thermoplast/glass interfaces. Computational materials science. 2000;19:223-8.
[17] Pang H. Mixed mode fracture analysis and toughness of adhesive joints. Engineering fracture mechanics. 1995;51:575-83.
[18] Warrior N, Pickett A, Lourenco N. Mixed- Mode Delamination–Experimental and Numerical Studies. Strain. 2003;39:153-9.
[19] Yang Q, Thouless M, Ward S. Numerical simulations of adhesively-bonded beams failing with extensive plastic deformation. Journal of the Mechanics and Physics of Solids. 1999;47:1337-53.
[20] Van den Bosch M, Schreurs P, Geers M. An improved description of the exponential Xu and Needleman cohesive zone law for mixed-mode decohesion. Engineering Fracture Mechanics. 2006;73:1220-34.
[21] Ortiz M, Pandolfi A. Finite-deformation irreversible cohesive elements for three-dimensional crack-propagation analysis. International Journal for Numerical Methods in Engineering. 1999;44:1267-82.
[22] Zhang ZJ, Paulino GH. Cohesive zone modeling of dynamic failure in homogeneous and functionally graded materials. International Journal of Plasticity. 2005;21:1195-254.
[23] Zeng X, Li S. A multiscale cohesive zone model and simulations of fractures. Computer methods in applied mechanics and engineering. 2010;199:547-56.
[24] Li S, Demirci E, Silberschmidt VV. Variability and anisotropy of mechanical behavior of cortical bone in tension and compression. Journal of the mechanical behavior of biomedical materials. 2013;21:109-20.
[25] Currey JD. The structure and mechanics of bone. Journal of Materials Science. 2012;47:41-54.

[26] Sverdlova NS, Witzel U. Principles of determination and verification of muscle forces in the human musculoskeletal system: muscle forces to minimise bending stress. Journal of biomechanics. 2010;43:387-96.
[27] Mercer C, He M, Wang R, Evans A. Mechanisms governing the inelastic deformation of cortical bone and application to trabecular bone. Acta Biomaterialia. 2006;2:59-68.
[28] Nyman JS, Leng H, Dong XN, Wang X. Differences in the mechanical behavior of cortical bone between compression and tension when subjected to progressive loading. Journal of the mechanical behavior of biomedical materials. 2009;2:613-9.
[29] Zhai J, Zhou M. Finite element analysis of micromechanical failure modes in a heterogeneous ceramic material system. International Journal of fracture. 2000;101:161-80.
[30] Roe K, Siegmund T. An irreversible cohesive zone model for interface fatigue crack growth simulation. Engineering fracture mechanics. 2003;70:209-32.
[31] Tvergaard V. Cohesive zone representations of failure between elastic or rigid solids and ductile solids. Engineering Fracture Mechanics. 2003;70:1859-68.
[32] Hughes TJ, Pister KS, Taylor RL. Implicit-explicit finite elements in nonlinear transient analysis. Computer Methods in Applied Mechanics and Engineering. 1979;17:159-82.
[33] Siegmund T, Allen MR, Burr DB. Failure of mineralized collagen fibrils: modeling the role of collagen cross-linking. Journal of biomechanics. 2008;41:1427-35.
[34] Haverty D, Tofail SAM, Stanton KT, McMonagle JB. Structure and stability of hydroxyapatite: density functional calculation and Rietveld analysis. Physical Review B. 2005;71:094103.
[35] Luo Q, Nakade R, Dong X, Rong Q, Wang X. Effect of mineral–collagen interfacial behavior on the microdamage progression in bone using a probabilistic cohesive finite element model. Journal of the mechanical behavior of biomedical materials. 2011;4:943-52.
[36] Rho J-Y, Kuhn-Spearing L, Zioupos P. Mechanical properties and the hierarchical structure of bone. Medical engineering & physics. 1998;20:92-102.
[37] Weiner S, Wagner HD. The material bone: structure-mechanical function relations. Annual Review of Materials Science. 1998;28:271-98.
[38] Weiner S, Traub W, Wagner HD. Lamellar bone: structure–function relations. Journal of structural biology. 1999;126:241-55.
[39] Ji B, Gao H. Mechanical properties of nanostructure of biological materials. Journal of the Mechanics and Physics of Solids. 2004;52:1963-90.
[40] Carden A, Rajachar R, Morris MD, Kohn D. Ultrastructural changes accompanying the mechanical deformation of bone tissue: a Raman imaging study. Calcified Tissue International. 2003;72:166-75.
[41] Tai K, Ulm F-J, Ortiz C. Nanogranular origins of the strength of bone. Nano letters. 2006;6:2520-5.
[42] Yamashita J, Li X, Furman BR, Rawls HR, Wang X, Agrawal C. Collagen and bone viscoelasticity: a dynamic mechanical analysis. Journal of biomedical materials research. 2002;63:31-6.
[43] Sasaki N, Enyo A. Viscoelastic properties of bone as a function of water content. Journal of Biomechanics. 1995;28:809-15.

[44] Wallace JM, Rajachar RM, Chen X-D, Shi S, Allen MR, Bloomfield SA, et al. The mechanical phenotype of biglycan-deficient mice is bone- and gender-specific. Bone. 2006;39:106-16.
[45] Du Q, Faber V, Gunzburger M. Centroidal Voronoi Tessellations: Applications and Algorithms. SIAM Review. 1999;41:637-76.
[46] Lin L, Wang X, Zeng X. Geometrical Modeling of Cell Division and Cell Remodeling Based on Voronoi Tessellation Method. CMES: Computer Modeling in Engineering & Sciences. 2014;98:203-20.
[47] Qin Z, Gautieri A, Nair AK, Inbar H, Buehler MJ. Thickness of hydroxyapatite nanocrystal controls mechanical properties of the collagen–hydroxyapatite interface. Langmuir. 2012;28:1982-92.
[48] Kohles SS, Martinez DA. Elastic and physicochemical relationships within cortical bone. Journal of biomedical materials research. 2000;49:479-88.
[49] McNally EA, Schwarcz HP, Botton GA, Arsenault AL. A model for the ultrastructure of bone based on electron microscopy of ion-milled sections. PLoS One. 2012;7:e29258.
[50] Sroga GE, Vashishth D. Effects of bone matrix proteins on fracture and fragility in osteoporosis. Current osteoporosis reports. 2012;10:141-50.
[51] Olszta MJ, Cheng X, Jee SS, Kumar R, Kim Y-Y, Kaufman MJ, et al. Bone structure and formation: a new perspective. Materials Science and Engineering: R: Reports. 2007;58:77-116.
[52] Zeng X, Li S. Application of a multiscale cohesive zone method to model composite materials. International Journal of Multiscale Computational Engineering. 2012;10:391-405.
[53] Li S, Zeng X, Ren B, Qian J, Zhang J, Jha AK. An atomistic-based interphase zone model for crystalline solids. Computer Methods in Applied Mechanics and Engineering. 2012;229:87-109.
[54] Lin L, Zeng X. Computational modeling and simulation of spall fracture in polycrystalline solids by an atomistic-based interfacial zone model. Engineering fracture mechanics. 2015;142:50-63.
[55] Lin L, Dhanawade R, Zeng X. Numerical simulations of dynamic fracture growth based on a cohesive zone model with microcracks. Journal of Nanomechanics and Micromechanics. 2014;4:B4014003.
[56] Ebacher V, Tang C, McKay H, Oxland TR, Guy P, Wang R. Strain redistribution and cracking behavior of human bone during bending. Bone. 2007;40:1265-75.
[57] Hengsberger S, Kulik A, Zysset P. Nanoindentation discriminates the elastic properties of individual human bone lamellae under dry and physiological conditions. Bone. 2002;30:178-84.
[58] Hoffler CE, Guo XE, Zysset PK, Goldstein SA. An application of nanoindentation technique to measure bone tissue lamellae properties. Journal of biomechanical engineering. 2005;127:1046-53.
[59] Dong XN, Almer JD, Wang X. Post-yield nanomechanics of human cortical bone in compression using synchrotron X-ray scattering techniques. Journal of biomechanics. 2011;44:676-82.
[60] Giri B, Almer JD, Dong XN, Wang X. In situ mechanical behavior of mineral crystals in human cortical bone under compressive load using synchrotron X-ray scattering techniques. Journal of the mechanical behavior of biomedical materials. 2012;14:101-12.

[61] Abdul-Baqi A, Van der Giessen E. Indentation-induced interface delamination of a strong film on a ductile substrate. Thin Solid Films. 2001;381:143-54.

Appendix A.Analytical solution derivation of stress-strain relation

In the analytical model shown inFig. 9 (a), the forces in y direction are in equilibrium:

$$\sum F_y = 0 \tag{A.1}$$

From the force balance in y axis, we have:

$$F_b = 2(F_n cos\theta + F_t sin\theta) \tag{A.2}$$

whereF_b is applied force;F_n and F_t are normal and shear force of interface, respectively; θ is the geometry angle of hexagon.

Substitute $F_b = \sigma_b A,\ F_n = \sigma_n A_s,\ F_t = \tau_s A_s\ ,\ A = 2A_s cos\theta$ into Eq.(A.2), we have:

$$\sigma_b = \sigma_n + \tau_s \frac{sin\theta}{cos\theta} \tag{A.3}$$

where σ_b is the bulk stress; σ_n represents interfacial normal compressive stress; τ_s denotes interfacial shear stress.

From Fig. 9(c)-(d), the sliding distance is determined to be:

$$\delta_s = \delta_{s1} + \delta_{s2} = \delta_l cos\theta + d_1 sin\theta \tag{A.4}$$

whered_1 is the compressed displacement along vertical direction and δ_l is opening displacement along horizontal direction.

Thus, from Eq.(A.4), the shear strainis provided as:

$$\gamma_s = \frac{\delta_s}{t_0} = \frac{(\delta_l cos\theta + d_1 sin\theta)}{t_0} \tag{A.5}$$

wheret_0 is the original thickness of interface.

Additionally, from the deformation geometry in Fig. 9(c), the following compatibility relations can be obtained:

$$d_1 + d_2 = t_0 cos\theta \qquad \text{(A.6)}$$

$$d_2 = \left(\frac{t_0}{2} + \delta_l\right) tan\alpha \qquad \text{(A.7)}$$

Based on the standard hexagon structure, from Fig. 9(c), the shear strain also can be described as:

$$\gamma_s = \frac{\pi}{2} - \theta - \alpha \text{where} \theta = \frac{\pi}{6} \qquad \text{(A.8)}$$

Substituting Eqs.(A.6)-(A.8) into Eq.(A.5) yields:

$$\gamma_s = \frac{\left[\left(\frac{d_2}{tan\left(\frac{\pi}{3}-\gamma_s\right)} - \frac{t_0}{2}\right)cos\theta + d_1 sin\theta\right]}{t_0} \text{(A.9)}$$

According to the trigonometric sum and difference formulas:

$$tan\left(\frac{\pi}{3} - \gamma_s\right) = \frac{sin\left(\frac{\pi}{3}-\gamma_s\right)}{cos\left(\frac{\pi}{3}-\gamma_s\right)} = \frac{\sin\left(\frac{\pi}{3}\right)cos\gamma_s - cos\left(\frac{\pi}{3}\right)sin\gamma_s}{\cos\left(\frac{\pi}{3}\right)cos\gamma_s + sin\left(\frac{\pi}{3}\right)sin\gamma_s} \qquad \text{(A.10)}$$

Under the small deformation assumption:

$$sin\gamma_s \sim \gamma_s, cos\gamma_s \sim 1 - \frac{{\gamma_s}^2}{2}$$

Eq.(A.10) yields the following relation:

$$tan\left(\frac{\pi}{3} - \gamma_s\right) \approx \frac{\sqrt{3} - \frac{\sqrt{3}}{2}{\gamma_s}^2 - \gamma_s}{1 + \sqrt{3}\gamma_s - \frac{{\gamma_s}^2}{2}} \quad \text{(A.11)}$$

Substituting Eq.(A.10) into Eq.(A.9), the shear strainis obtainedas:

$$\gamma_s = \frac{\sqrt{4t_0^2 - 2\sqrt{3}t_0 d_2} - t_0}{\sqrt{3}t_0} \qquad \text{(A.12)}$$

From Fig. 9(c)-(d) and Eq.(A.5), the deformed interfacial thickness isdeterminedas:

$$t = \delta_s tan\theta + \frac{d_2}{cos\theta} = \gamma_s t_0 tan\theta + \frac{d_2}{cos\theta} \qquad \text{(A.13)}$$

The compressed distance in normal direction of interfacial surfaceis defined as:

$$\delta_{nn} = t_0 - t = t_0 - \gamma_s t_0 tan\theta - \frac{d_2}{cos\theta} \text{(A.14)}$$

According to Hooke's law, the compressive normal stress and shear stress are obtained as:

$\sigma_n = E_n \varepsilon_n = E_n \frac{\delta_{nn}}{t_0}$(A.15)

$$\tau_s = G_s \gamma_s = G_s \frac{\delta_s}{t_0} \text{(A.16)}$$

whereE_n represents the normal modulus of interface and G_s is the shear modulus of interface.

Substitute Eq.(A.14), (A.15) and (A.16) into Eq.(A.1) yields:

$\sigma_b = \frac{E_n}{t_0}\left(t_0 - \gamma_s t_0 tan\theta - \frac{d_2}{cos\theta}\right) + G_s \gamma_s tan\theta$(A.17)

From Fig. 9(c), the bulk strain can bewritten as:

$\varepsilon_b = \frac{d_1}{h_0}$where$h_0$ is the original height of specimen (A.18)

Thus, from Eq.(A.6), (A.12),(A.17) and (A.18), the stress-strain relation can be easily obtained:

$$\sigma_b = E_n \left(\frac{h_0 \varepsilon_b}{t_0 cos\theta} - \frac{\sqrt{4t_0^2 - 2\sqrt{3}t_0(t_0 cos\theta - h_0 \varepsilon_b)} - t_0}{\sqrt{3}t_0} tan\theta \right) + G_s \frac{\sqrt{4t_0^2 - 2\sqrt{3}t_0(t_0 cos\theta - h_0 \varepsilon_b)} - t_0}{\sqrt{3}t_0} tan\theta \text{(A.19)}$$